Rare Metal Materials and Engineering
Volume 55, Issue 7, July 2026
Available online at www.rmme.ac.cn

Science Press

Cite this article as: An Jiazhi, Liu Quanfeng, Ding Wanwu, et al. Microstructure, Mechanical Properties and Wear Resistance of ($Ti_2Al_{20}La$+Al_3Ti)/Al-7Si Composites[J]. Rare Metal Materials and Engineering, 2026, 55(07): 1641-1650. DOI: https://doi.org/10.12442/j.issn.1002-185X.20250374.

ARTICLE

Microstructure, Mechanical Properties and Wear Resistance of ($Ti_2Al_{20}La$+Al_3Ti)/Al-7Si Composites

An Jiazhi[1,2], Liu Quanfeng[1,2], Ding Wanwu[1,2], Wei Guoli[3], Yu Haicun[1,2], Yang Chengliang[3]

[1] School of Metallurgy and Environment, Lanzhou University of Technology, Lanzhou 730050, China; [2] State Key Laboratory of Advanced Processing and Recycling of Nonferrous Metals, Lanzhou University of Technology, Lanzhou 730050, China; [3] Jiuquan Iron and Steel (Group) Co., Ltd, Jiayuguan 735100, China

Abstract: ($Ti_2Al_{20}La$+Al_3Ti)/Al-7Si composites rich in $Ti_2Al_{20}La$ and Al_3Ti reinforcement phases were prepared by the melt blending method. The influence of the addition amount of Al-Ti-La alloy on the microstructure, mechanical properties, and wear resistance of the composites was analyzed. Results reveal that the ($Ti_2Al_{20}La$+Al_3Ti)/Al-7Si composite (adding 10wt% Al-Ti-La alloy into the Al-7Si alloy) is composed of fine α-Al grains, short rod-like eutectic Si, and blocky Al_3Ti and $Ti_2Al_{20}La$ phases. The tensile strength, elongation, and hardness of the composite are 176.9 MPa, 11.62%, and 73.2 HV, increased by 13.4%, 57.0%, and 26.2% compared with those of the Al-7Si alloy, respectively. It is suggested that the ($Ti_2Al_{20}La$+Al_3Ti)/Al-7Si composite exhibits relatively high plasticity. Furthermore, the wear resistance of the composites is increased by 20.1%. The performance enhancement is attributed to two key mechanisms. One is the formation of Al_3Ti transition layer at the interface between the Al_3Ti reinforcement phase and the aluminum matrix, which establishes a semi-coherent relationship with Al_3Ti phase. The other is the adsorption of element Si by element La within the $Ti_2Al_{20}La$ reinforcement phase, leading to Si enrichment at the edges of the $Ti_2Al_{20}La$ phase and thereby forming a semi-coherent Si layer.

Key words: aluminum matrix composites; Al-Ti-La alloys; mechanical properties; wear resistance

1 Introduction

Metal matrix composites (MMCs) have attracted considerable attention due to their excellent mechanical, thermal, and electrical properties[1–2]. In comparison with the traditional alloys, MMCs are generally characterized by superior strength-to-mass ratios and performance-to-cost ratios[3]. They also have the advantages of low density, high strength, and good toughness. Therefore, MMCs are considered as lightweight high-performance materials[4–8].

Traditional ceramic reinforcements, such as boron carbide (B_4C), silicon carbide (SiC), alumina (Al_2O_3), and carbon-based reinforcements, i. e., carbon nanotubes (CNTs) and graphene, have been used to improve the mechanical properties and to strengthen the aluminum-metal matrix composites. Yang et al[6] prepared (SiO_2+Al_2O_3)/Al-7Si composites and found that the increase in SiO_2 and Al_2O_3 contents in the composites increases the tensile strength and hardness of the material, but the generated pores affect the elongation. Shah et al[7] found that TiB_2 has a significant enhancement effect on the strength and hardness of A356 alloy, but the elongation enhancement of the composites is not significant. Hence, the concern is that the addition of conventional reinforcing phases impairs the ductility and fracture toughness of aluminum-based matrix composites[8–10]. However, rare earth elements have a positive effect on the plasticity and mechanical properties. Sharma et al[11] prepared (CeO_2+SiC)/6061Al composites by stir casting process, and the results showed that after the addition of 2.5wt% CeO_2, the tight interfacial bonding between cerium oxide and aluminum matrix increases the tensile strength from 30 MPa to 123 MPa,

Received date: July 19, 2025
Foundation item: National Natural Science Foundation of China (52161006); Industrial Support Plan Project of Gansu Provincial Department of Education (2021CYZC-23); Central Guidance for Local Scientific and Technological Development Funding Projects (23ZYQB309); Gansu Provincial Science and Technology Major Project (22ZD6GB019); Lanzhou Youth Science and Technology Talent Innovation Project (2024-QN-106)
Corresponding author: Ding Wanwu, Ph. D., Professor, School of Metallurgy and Environment, Lanzhou University of Technology, Lanzhou 730050, P. R. China, E-mail: dingww@lut.edu.cn

and the hardness is increased by 33.8%. Sharma et al[12] also added 6wt% SiC and 2wt% CeO_2+La_2O_3 to 6061Al composite by stir casting process, and the results showed that the addition of rare earth oxides greatly improves the tensile strength and elongation of the material, and the wear resistance is increased by 89.40%. Besides, aluminum matrix composites are widely used in the manufacture of mild steel bearings, such as gear parts, brake drums, piston tops, crankshafts, and cylinder blocks, due to their outstanding wear resistance[13]. Shivamurthy et al[14] studied the dry friction and wear properties of A356 aluminum alloy and aluminum matrix composites reinforced by 10wt% – 20wt% SiC_p particles. The results showed that the addition of SiC_p reinforced particles significantly improves the wear resistance of A356 alloy, and with the increase in volume fraction of SiC_p reinforced particles, the wear rate is decreased and the wear resistance is improved.

As for the rare earth elements, the investigation of the relationship between La atom radius and orientation shows great research potential of low-cost La for the refinement and transformation of aluminum alloys[15]. Xu et al[16] demonstrated that the addition of the trace addition of element La can transform the Al_3Ti crystal structure of DO_{22} type into a cubic structure, thereby increasing the fracture toughness of the modified composite material by 143.75%. Peng et al[17] reported that $Ti_2Al_{20}La$ exhibits superior fine-grain strengthening properties and refinement efficiency in comparison to Al_3Ti. Ding et al[18] prepared a novel Al-Ti-La master alloy, which is rich in $Ti_2Al_{20}La$ phase, and the $Ti_2Al_{20}La$ phase exerted a substantial fine-grain strengthening effect on Al-Si alloys. The fracture mode transitioned from transgranular to intergranular fracture, resulting in a 104.8% increase in elongation. It is suggested that Al-Ti-La alloys possess considerable potential for the strengthening of hypoeutectic Al-Si alloys. This suggestion is primarily attributed to the active effect of the rare earth element La, which is released from the $Ti_2Al_{20}La$ phase, on eutectic silicon. Conversely, the $Ti_2Al_{20}La$ phase within the Al-Ti-La alloy has the capacity to refine the grains, thereby significantly enhancing the overall properties of the material.

Therefore, in this research, the melt blending method was used to prepare ($Ti_2Al_{20}La$+Al_3Ti)/Al-7Si composites, which are rich in $Ti_2Al_{20}La$ and Al_3Ti reinforcement phases. The microstructure, mechanical properties, and wear resistance of the composites were investigated.

2 Experiment

The raw materials used in this study were industrially pure aluminum, Al-10Si, aluminum powder, titanium powder, and lanthanum blocks. The Al-Ti-La alloy was firstly prepared by in-situ synthesis based on the method in Ref. [18]. The raw materials of pure aluminum, Al-10Si, and Al-Ti-La master alloy were cleaned, weighed, and then placed into a crucible. The addition amount of Al-Ti-La master alloy was chosen as 0.0wt%, 7.7wt%, 10.0wt%, 12.5wt%, 16.7wt%, 25.0wt%, 33.4wt%, and 50.0wt%. The designation and composition of all samples in this research are listed in Table 1.

The matrix material was melted using a silicon carbide resistance furnace with the temperature maintained above 720 °C in order to compensate for the heat loss during stirring and to improve wettability and pouring performance. Subsequently, the reinforcement material (Al-Ti-La alloy) was preheated in a drying oven at approximately 200 °C for about 1 h. This preheating process is essential for removing the residual moisture, thereby enhancing the wettability between the reinforcement material and the matrix.

After thorough stirring, the molten mixture was cooled to 700 °C and cast into a metal mould with 80 mm in length and 10 mm in diameter. Then, it was preheated at 200 °C for 30 min and cooled naturally to room temperature. The mixing and casting processes are illustrated in Fig.1.

The sample was polished using SiC sandpaper of 320#, 400#, 800#, 1000#, and 2000# in turn. Then, the sample was polished by diamond grinding paste with particle size of 3, 1, and 0.25 μm to obtain a mirror finish.

The microhardness of the sample was tested using a Wilson VH1102 microhardness tester. The prepared macroscopic round sample was ground and polished until no scratches were visible, and the requirements were the same as the ones for the preparation of metallographic samples. Take 10 measurement points with equal intervals on the surface of each sample for hardness testing. The load was 0.1 HV, and the loading time was 30 s. Then, after removing the lowest and highest hardness values, the average value of the remaining 8 hardness values was used for analysis to reduce errors and to obtain the Vickers hardness value of the material.

According to GB/T228. 1-2010 standard, the rod-shaped sample was processed into a specific tensile test specimen, as shown in Fig. 2. The mechanical properties were tested on an AG-10TA electronic universal testing machine at a tensile rate of 0.5 mm/min. At least three tensile tests were performed on each group of tensile specimens, and the average value was taken as the tensile result for analysis. After the sample was broken, it was placed in a centrifuge tube containing alcohol to prevent oxidation from the air, so the fracture surface could be kept for the subsequent observation by scanning electron microscope (SEM).

The tribological properties were evaluated under dry sliding conditions using a multi-function reciprocating tribometer

Table 1 Designation and composition of samples (wt%)

Sample	Al-Ti-La	Ti	La	Si	Al
0#	0.0	0.00	0.00	7.00	Bal.
1#	7.7	0.23	0.34	6.46	Bal.
2#	10.0	0.30	0.43	6.30	Bal.
3#	12.5	0.38	0.54	6.12	Bal.
4#	16.7	0.50	0.73	5.83	Bal.
5#	25.0	0.75	1.09	5.25	Bal.
6#	33.4	1.00	1.45	4.66	Bal.
7#	50.0	1.50	2.18	3.50	Bal.

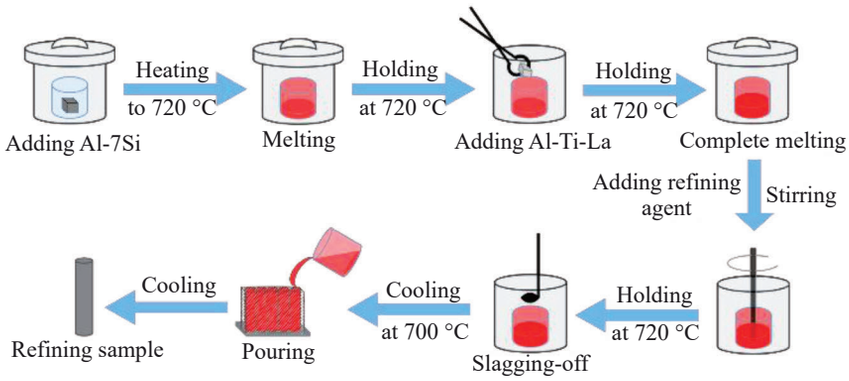

Fig.1 Schematic diagram of mixing and casting processes

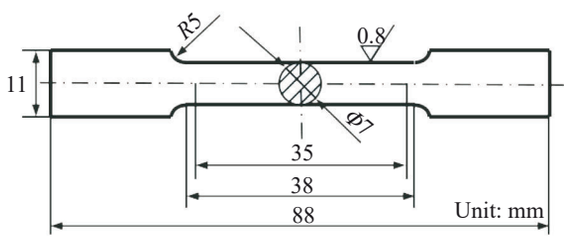

Fig.2 Schematic diagram of tensile test specimen

(Multi Function Tribometer MFT-5000). The tribological analysis employed a 45-type steel ball with 6 mm in diameter as the upper sample. The tribological test was conducted at the load of 5, 10, 15, and 20 N with a sliding frequency of 2 Hz and a total sliding distance of 3000 m. The tribological test was conducted at room temperature. After each test, the table was fixed again, and a new upper pattern was used to eliminate any wear debris that might adhere to the disc or sample. Before each test, the upper pattern was examined to ascertain the effective contact between the upper pattern surface and the steel disc. The objective of this investigation was to examine the effects of the content of Al-Ti-La intermetallic compound and the applied normal load on the friction coefficient of materials.

The experiment employed a Bruker D8 X-ray diffractometer (XRD) to analyze the potential phases in the sample. Cu Kα radiation (λ=0.154 156 nm) was used in the experiment with acceleration voltage of 40 kV, emission current of 100 mA, scanning speed of 4°/min, diffraction angle (2θ) range of 20°–90°, and scanning step of 0.02°. The experiment data were processed using the professional software Jade 9 for qualitative phase analysis. The obtained diffraction peaks were then compared with the standard PDF card to identify the relevant phases. In this experiment, the microstructural characteristics of the composites modified by Al-Ti-La alloy of different contents were observed using an Axio Scope A1 optical microscope (OM). To perform qualitative and quantitative analyses of specific small areas and strengthening phases, a Quanta FEG-450 field emission SEM and a Tescan Mira 3 field emission SEM were used. Both SEMs were equipped with energy dispersive spectrometer (EDS). The Nano Measurer 1.2 was used to determine the dimensions of α-Al and eutectic Si. The average grain size of α-Al was calculated as $[(L_1+L_2+L_3+L_4)/4+\cdots\cdots+(L_n+L_{n+1}+L_{n+2}+L_{n+3}+L_{n+4})/4]/n$, and the average size of eutectic Si was calculated as $(L'_1+L'_2+\cdots\cdots+L'_n)/n$, where L is the grain size of α-Al, L' is the grain size of eutectic Si, and the subscript n (n=1, 2, 3……) is mark number. Fig.3 shows the schematic diagram of grain size measurement.

3 Results and Discussion

3.1 Phase composition and microstructure of composites

Fig.4 shows XRD patterns of 0#–7# samples. It can be seen that the primary secondary phases of 1#–7# samples are Al_3Ti, $Ti_2Al_{20}La$, and a minor amount of $Al_{11}La_3$.

Fig.5 shows OM microstructures and grain size of α-Al of 0#–7# samples. Fig.5a displays OM microstructure of Al-7Si alloy (0# sample). The α-Al in the Al-7Si alloy exhibits a petal-like morphology with comparatively substantial dendrites. It is widely acknowledged that the anisotropic growth of petal-like α-Al has the potential to exert a deleterious effect on the mechanical properties of material[19]. After the addition of Al-Ti-La alloy, the morphology of α-Al changes significantly. The majority of the large dendrites are transformed into fine equiaxed grains and some small dendrites, as illustrated in Fig.5b–5h. In the 0# sample, the spacing of the secondary dendrite arms (grain size) of α-Al reaches 56.1 μm. With the addition of the Al-Ti-La alloy, some α-Al is transformed into fine equiaxed crystals, the grain

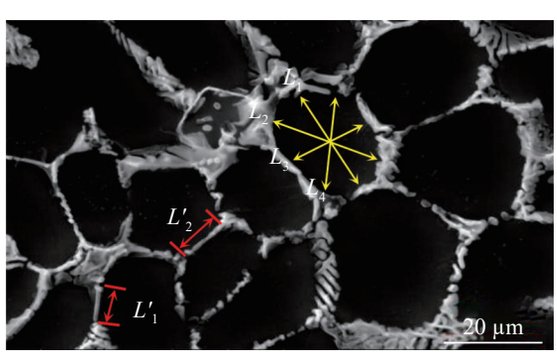

Fig.3 Schematic diagram of grain size measurement

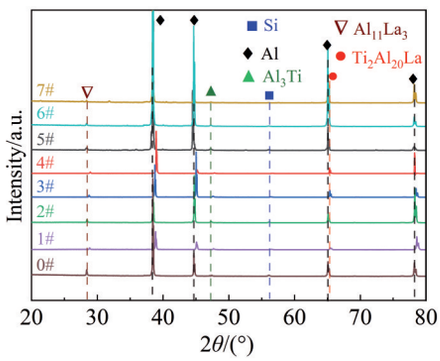

Fig.4 XRD patterns of 0#–7# samples

size of α-Al is decreased, and the smallest grain size of α-Al reaches 25.7 μm. For the 2# sample, the α-Al has a length of 31.6 μm. This phenomenon can be attributed to the refining effect of $Ti_2Al_{20}La$ and Al_3Ti phases, which act as heterogeneous nucleation sites. Additionally, some $Ti_2Al_{20}La$ phases dissolve, resulting in La atoms accumulating at the edges of the α-Al growth dendrites. This phenomenon further inhibits the growth of α-Al and refines the grains. This finding is consistent with the conclusions from Ref. [20 – 21]. Furthermore, with the increase in Al-Ti-La alloy content, the size of the $Ti_2Al_{20}La$ phase is gradually increased from the initial value of about 5 μm to about 100 μm, as shown in Fig.5f–5h. The refinement effect is markedly deteriorated with the increase in $Ti_2Al_{20}La$ phase size[22].

Fig.6 shows SEM microstructures and grain size of eutectic Si of 0# – 7# samples. The eutectic Si in the 0# sample is characterized by the predominance of coarse slabs and sharp needles, presenting the potential to induce stress concentration, leading to the formation of crack sources, and exerting a cutting effect on the matrix. This effect is evident in Fig. 6a. With the increase in Al-Ti-La alloy content, the eutectic Si undergoes a significant metamorphic transformation from the initial needle-like shape with a length of 17.00 μm to a rod-like shape with a length of 3.44 μm, as depicted in Fig. 6a – 6h. For the 2# sample, the eutectic Si of rod-like shape has a length of 8.78 μm. This is primarily because some $Ti_2Al_{20}La$ phases cannot easily dissolve in the α-Al phase and eutectic Si phase. Furthermore, the atomic radius and relative atomic mass of La are greater than those of Al and Si atoms. As a result, the La atoms distributed at the

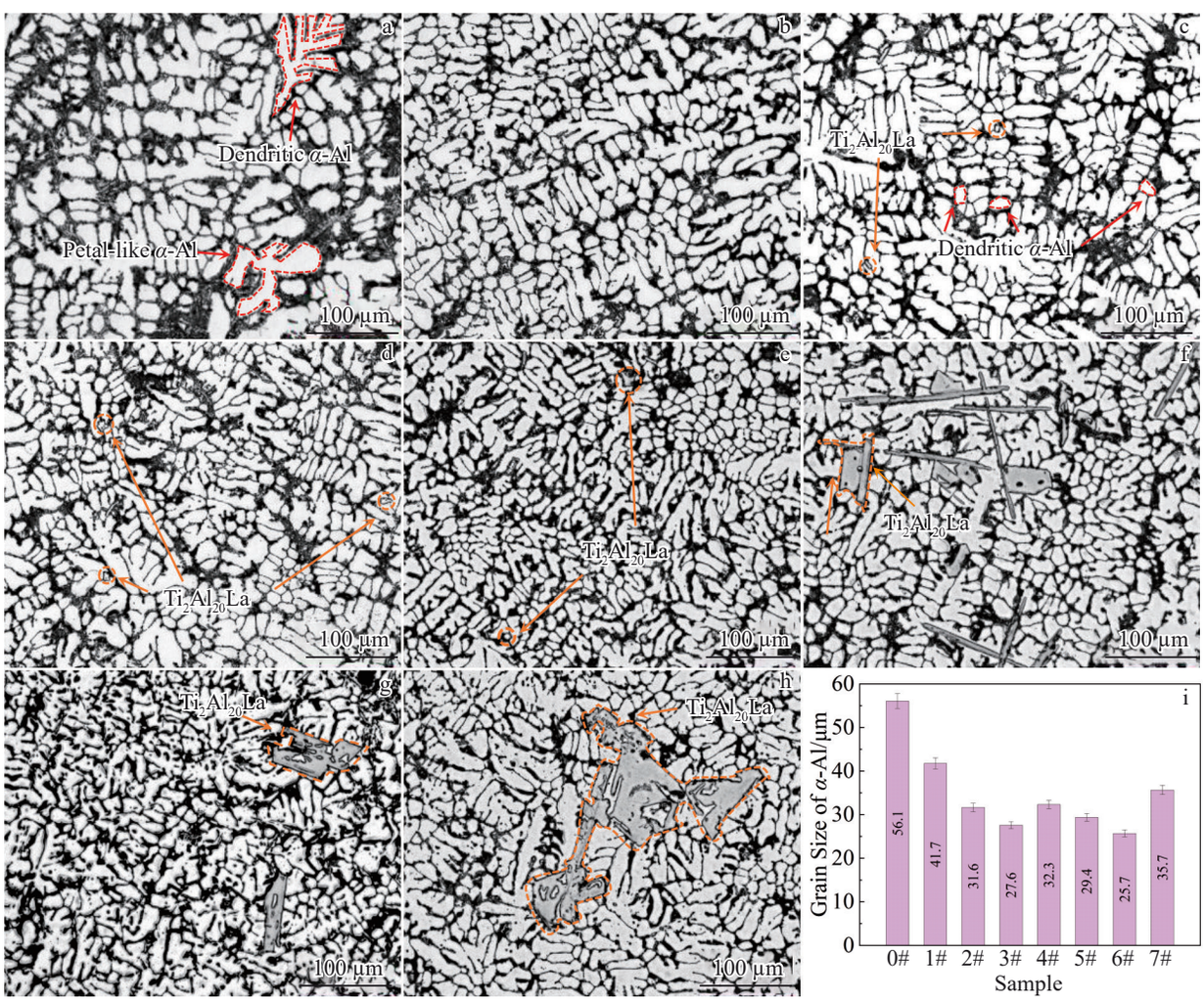

Fig.5 OM microstructures of 0# (a), 1# (b), 2# (c), 3# (d), 4# (e),5# (f), 6# (g), and 7# (h) samples; grain sizes of α-Al in 0#–7# samples (i)

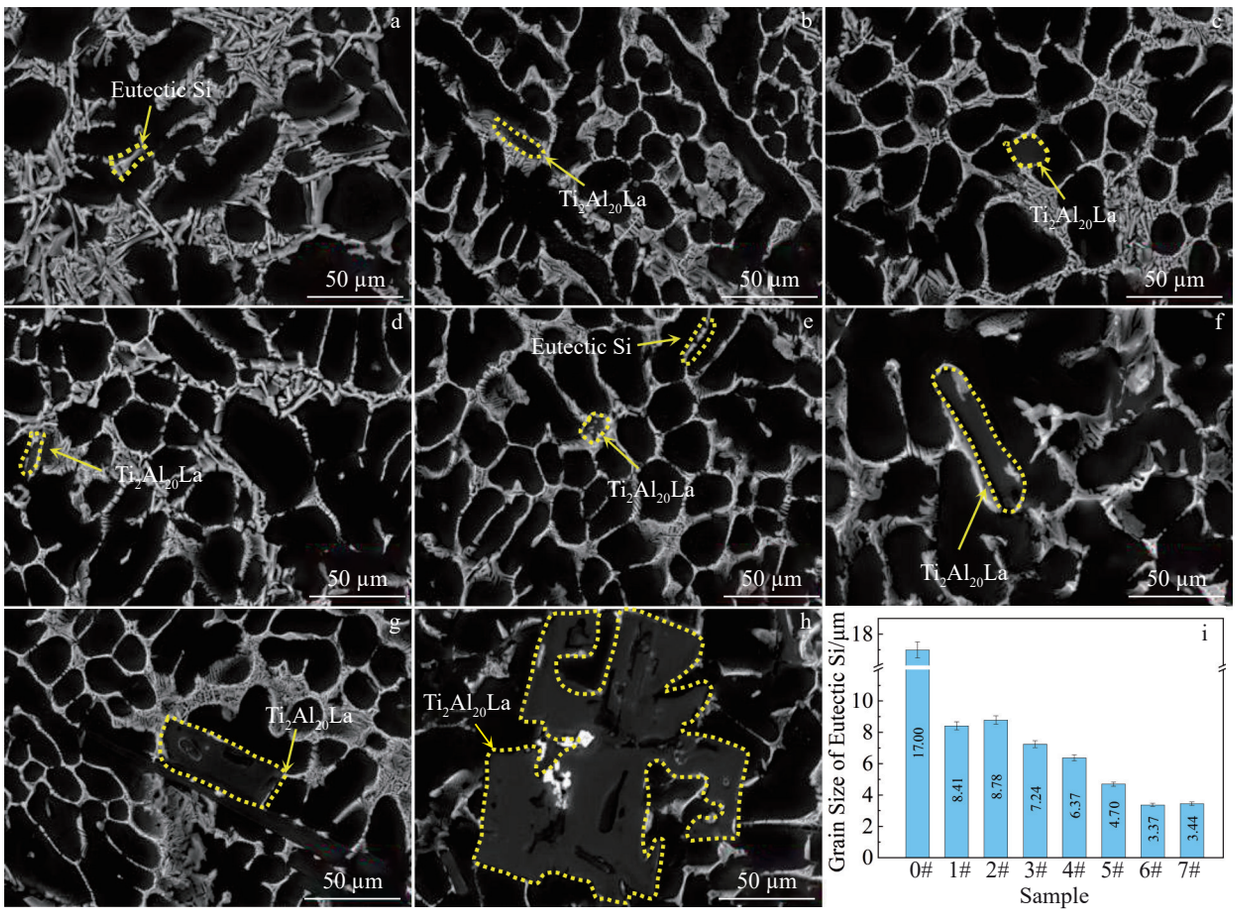

Fig.6 SEM microstructures of 0# (a), 1# (b), 2# (c), 3# (d), 4# (e),5# (f), 6# (g), and 7# (h) samples; grain sizes of eutectic Si in 0#–7# samples (i)

solidification front inhibit the growth of Si[23]. Furthermore, it is observed that with the increase in Al-Ti-La alloy content, the size of $Ti_2Al_{20}La$ phase in the ($Ti_2Al_{20}La$+Al_3Ti)/Al-7Si composite is also gradually increased, as demonstrated in Fig. 6f–6h. Qiu et al[24] reported that the presence of larger secondary phases is associated with the increased propensity for crack formation due to stress concentration.

3.2 Mechanical properties and fracture mechanism of composites

The mechanical properties of hypoeutectic Al-Si-based composites are governed by two critical factors. One is that the grain sizes of eutectic Si and α-Al play a significant role. Compared with sharp needle-like eutectic Si, round granular eutectic Si mitigates matrix cracking by reducing stress concentration. Additionally, finer α-Al grains facilitate stress distribution across a larger number of grains, thereby preventing localized stress accumulation and crack initiation. Furthermore, the tortuous and interlocking grain boundaries effectively hinder the crack propagation. The other factor is that the size and distribution of reinforcement phases are equally crucial. Large-sized and agglomerated reinforcement phases tend to act as stress concentrators, serving as potential crack initiation sites and ultimately degrading the mechanical performance of the materials[21]. Fig. 7 shows the stress-strain curves of 0#–7# samples, and Table 2 shows the mechanical properties of 0#–7# samples. It can be seen that the 0# sample exhibits a ultimate tensile strength of 156.0 MPa, an elongation of 7.40%, and a hardness of 58.0 HV. The 2# sample (containing 10wt% Al-Ti-La alloy) exhibits the highest elongation and ultimate tensile strength, reaching 11.62% and 176.9 MPa, respectively. Compared with those of 0# sample, the ultimate tensile strength and elongation of 2# sample increase by 13.4% and 57.0%, respectively. The hardness of the 2# sample is 73.2 HV, which is increased by 26.2%, compared with that of 0# sample. In order to more accurately

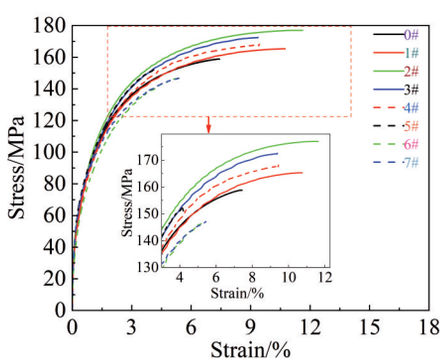

Fig.7 Stress-strain curves of 0#–7# samples

measure the comprehensive mechanical properties of the material, the quality index Q[23] is introduced, as follows:

$$Q=\mathrm{UST}+\alpha\lg(\mathrm{EI}) \quad (1)$$

where the parameter α is defined as 150 MPa; UTS and EI are abbreviations for ultimate tensile strength and elongation, respectively. The quality index Q of each sample can be calculated, and the results are demonstrated in Table 2. It can be seen that the quality index Q of 2# sample is the highest as 336.6 MPa, which is 17.6% higher than that of 0# sample (286.3 MPa).

Fig. 8 presents the tensile fracture surfaces of 0#, 1#, 2#, and 7# samples. As shown in Fig. 8a, the 0# sample exhibits prominent elongated dimples and extensive cleavage facets, indicating a predominantly brittle fracture mode. This behavior arises from stress concentration at coarse eutectic Si particles, which act as preferential crack propagation paths through transgranular fracture[23]. The introduction of a minor content of Al-Ti-La alloy results in reduced cleavage plane and shortened dimple lengths (Fig. 8b), suggesting partial suppression of brittle failure mechanism. Notably, the 2# sample shows a mixed fracture mode characterized by tear ridges and equiaxed dimples (Fig. 8c), reflecting enhanced ductility through refined eutectic Si and improved interfacial bonding. Conversely, excessive Al-Ti-La addition degrades mechanical performance due to the agglomeration of $Ti_2Al_{20}La$ phase (Fig. 8d). The yellow dashed region highlights the crack initiation phenomenon at the clustered $Ti_2Al_{20}La$ particles, while blocky dimples further infer the localized stress concentration and premature fracture at the phase boundaries.

Table 2 Mechanical properties of 0#–7# samples

Sample	Elongation/ %	Ultimate tensile strength/MPa	Hardness/ HV	Quality index, Q/MPa
0#	7.40	156.0	58.0	286.3
1#	10.74	165.3	72.5	319.9
2#	11.62	176.9	73.2	336.6
3#	9.37	172.5	74.2	318.2
4#	9.43	168.0	75.0	314.1
5#	5.47	146.3	72.5	256.9
6#	4.12	152.7	73.1	244.9
7#	5.45	147.1	75.0	257.5

Fig. 9 shows cross-section and longitudinal-section fracture surfaces of 6# sample and corresponding EDS analysis results. The phase at the bottom of the pit (point 1 in Fig. 9a) is identified as $Ti_2Al_{20}La$ phase with the Ti:Al:La ratio of 2:20:1. EDS analysis result at point 2 in Fig. 9c demonstrates the presence of a substantial quantity of $Ti_2Al_{20}La$ phase. The combination of the characteristics of cross-section and longitudinal-section of the tensile fracture of 6# sample indicates that during the tensile process, the coarse $Ti_2Al_{20}La$ phase is prone to stress concentration and crack generation. Furthermore, excessive stress concentration causes the formation of microcracks within the $Ti_2Al_{20}La$ phase.

3.3 Wear resistance of composite materials

Fig. 10 shows the confocal wear trace profiles and coefficient of friction (COF) curves under normal load of 20 N of 0# and 2# samples. It can be seen that the 0# sample displays a wear scar with depth of 152.2 μm, while the 2# sample demonstrates a significantly reduced depth of 121.3 μm, corresponding to a 20% enhancement in wear resistance. This improvement can be attributed to the refined microstructure and effective load-bearing capacity of the

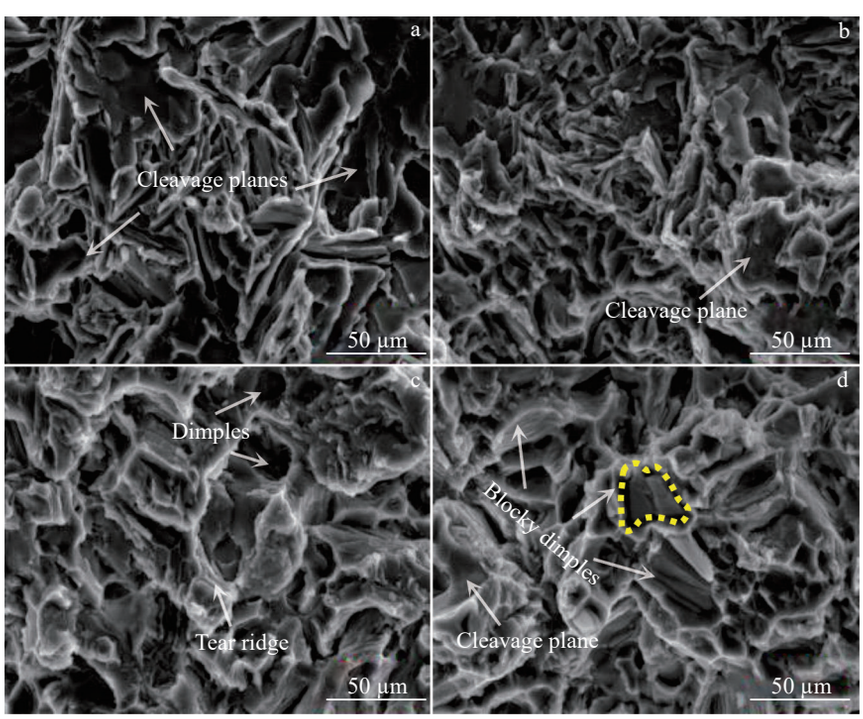

Fig.8 Tensile fracture surfaces of 0# (a), 1# (b), 2# (c), and 7# (d) samples

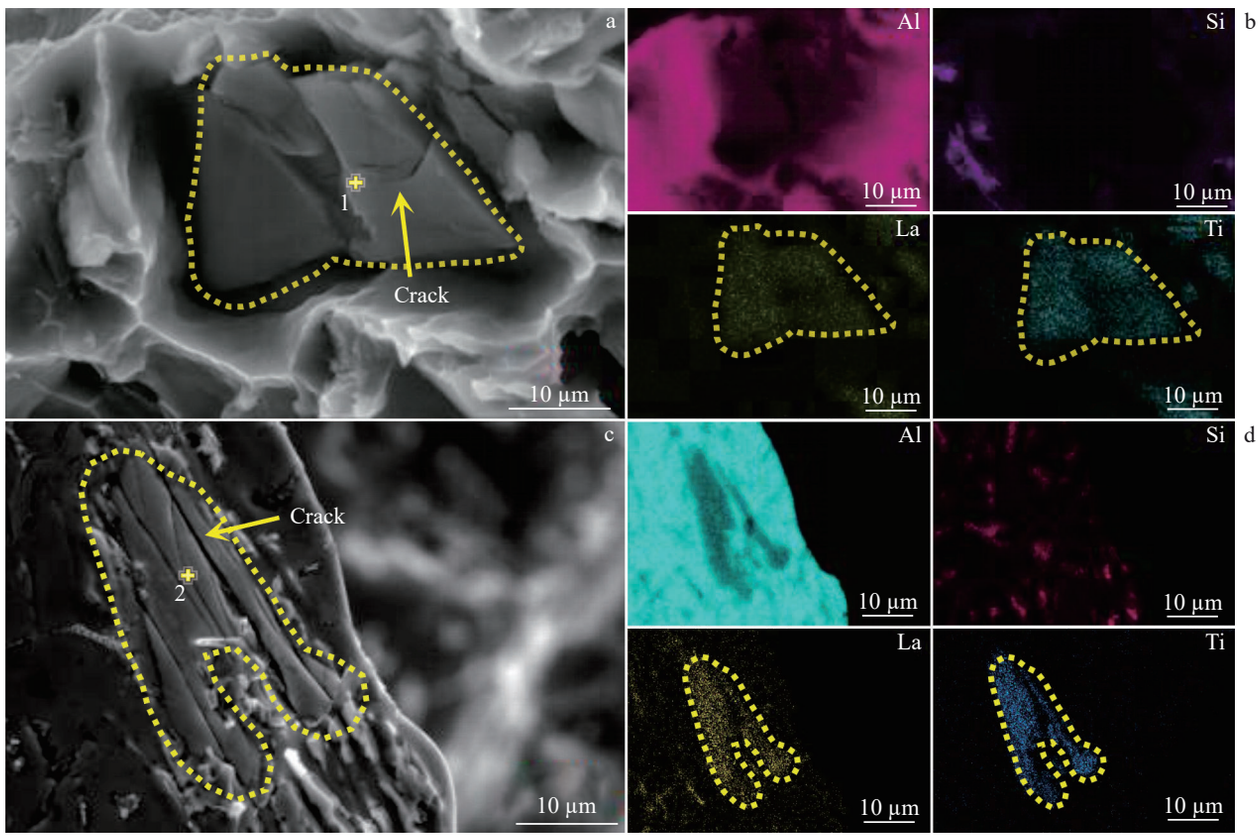

Fig.9 Cross-section (a) and longitudinal-section (c) fracture surfaces of 6# sample; EDS element mappings corresponding to Fig.9a (b) and Fig.9c (d)

reinforcement phases. Besides, the 0# sample exhibits pronounced fluctuations of COF curve (0.600–0.850) with an average COF value of 0.725, indicating the unstable interfacial interactions during sliding. In contrast, the 2# sample shows a relatively stabilized COF curve (average COF value of 0.620) with minimal amplitude variation, suggesting the enhanced interfacial compatibility and reduced localized stress accumulation. These results jointly indicate the superior tribological performance of the composite system.

However, when the $Ti_2Al_{20}La$ phase becomes coarser, its bonding with the matrix significantly weakens. During the wear process, particularly under fatigue wear or high-load

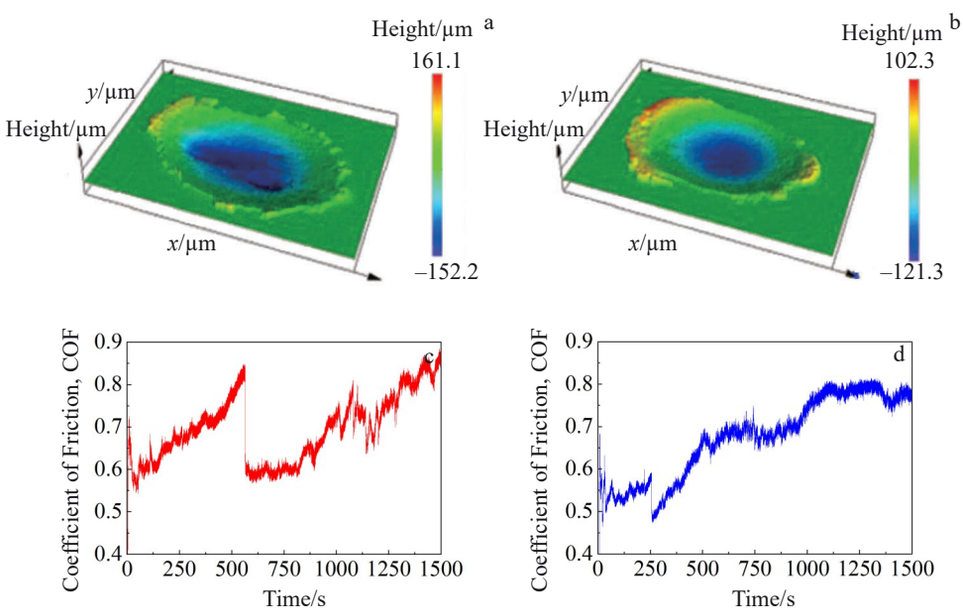

Fig.10 Confocal wear trace profiles (a–b) and COF under normal load of 20 N (c–d) of 0# (a, c) and 2# (b, d) samples

conditions, these phases may fracture due to their brittleness or detach entirely from the matrix, thereby accelerating the wear process[25].

3.4 Analysis of strengthening mechanism

Transmission electron microscope (TEM) coupled with selected area electron diffraction (SAED) analysis was used for further analysis. Fig. 11a–11b show TEM images of Al_3Ti phase and Al_3Ti transition layer in 2# sample, respectively. The interface between Al_3Ti phase and the aluminum substrate can be observed in Fig. 11a. According to EDS analysis results in Table 3, the materials at points P4, P5, and P6 are identified as the Al_3Ti phase, aluminum base material, and eutectic Si phase, respectively. Fig. 11b demonstrates the presence of a transition layer at the interface between Al_3Ti and the aluminum matrix. Fig. 11c illustrates SAED pattern of the transition layer, thereby confirming the presence of Al_3Ti. According to Fig. 11d, the (002) crystal plane spacing of Al_3Ti phase is 0.4113 nm, while the corresponding Al_3Ti (111) lattice spacing of the transition layer is 0.2070 nm. These two spacing results show a 2: 1 relationship, i. e., the transition layer and Al_3Ti show a half-coherent relationship. This is primarily attributable to the substantial internal stress at the interface between Al_3Ti and the aluminum substrate during the high-temperature preparation stage, leading to the formation of dislocation defects and lattice distortions. Pang et al[26] found that a nanoscale Al_3Ti transition layer significantly improves the elongation and shear strength. Furthermore, Pu[27] and Lu[28] et al demonstrated that the formation of a transition layer enhances the interfacial bonding strength between Al_3Ti and the aluminum substrate, thereby maintaining the structural stability and significantly improving the mechanical properties of the materials.

Table 3 EDS analysis results of points P1–P6 in Fig. 11–Fig. 12 (at%)

Point	Al	Si	Ti	La
P1	64.04	11.79	24.17	0.00
P2	99.45	0.39	0.17	0.00
P3	4.84	94.96	0.20	0.00
P4	99.49	0.37	0.07	0.07
P5	64.99	34.89	0.03	0.09
P6	85.44	0.00	9.63	4.93

Fig. 12 shows the microstructure of the interface between the $Ti_2Al_{20}La$ phase and the aluminum matrix. A clear enrichment of Si can be observed at the interface between the two phases. Shibata et al[29] reported that the element La possesses specific adsorption sites capable against adjacent Si. Consequently, Si near the interface between the $Ti_2Al_{20}La$ phase and the aluminum matrix exhibits a tendency to be enriched in the marginal region. As shown in Fig. 12, the (100) crystal plane of the Si layer exhibits semi-coherence with the $(1\bar{1}\bar{1})$ crystal plane of the $Ti_2Al_{20}La$ phase. Kuang et al[30] reported that the semi-coherent interface provides optimal lattice matching and enhances the interfacial bonding. This is

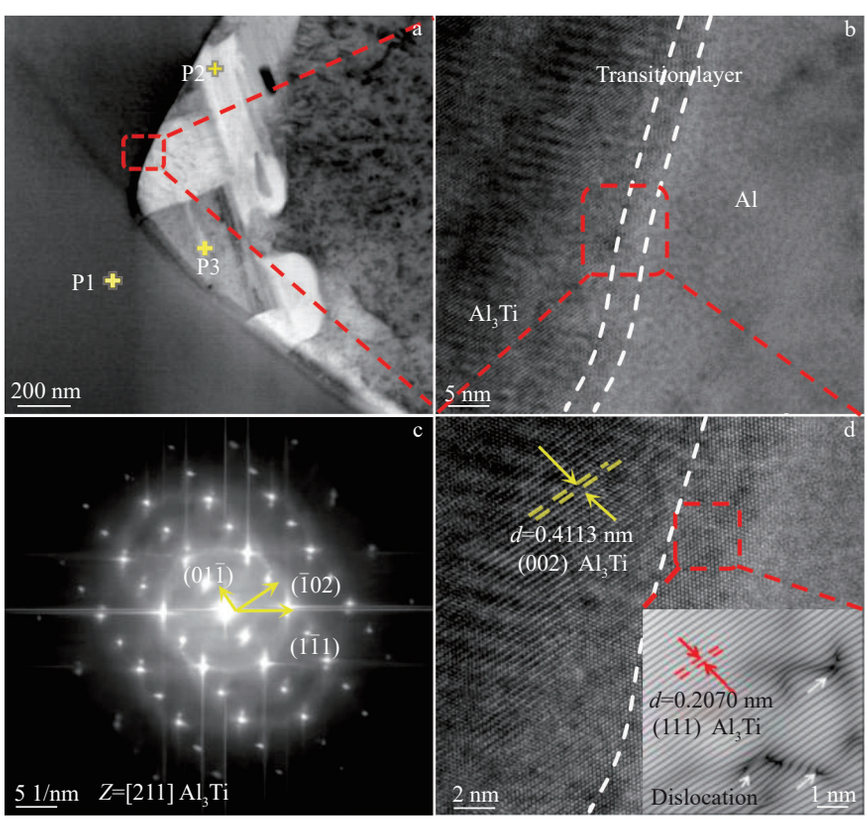

Fig.11 TEM images of Al_3Ti phase (a) and Al_3Ti transition layer (b) in 2# sample; SAED pattern of Al_3Ti transition layer (c); high-resolution TEM microstructure and corresponding inverse fast Fourier transform pattern of Al_3Ti transition layer (d)

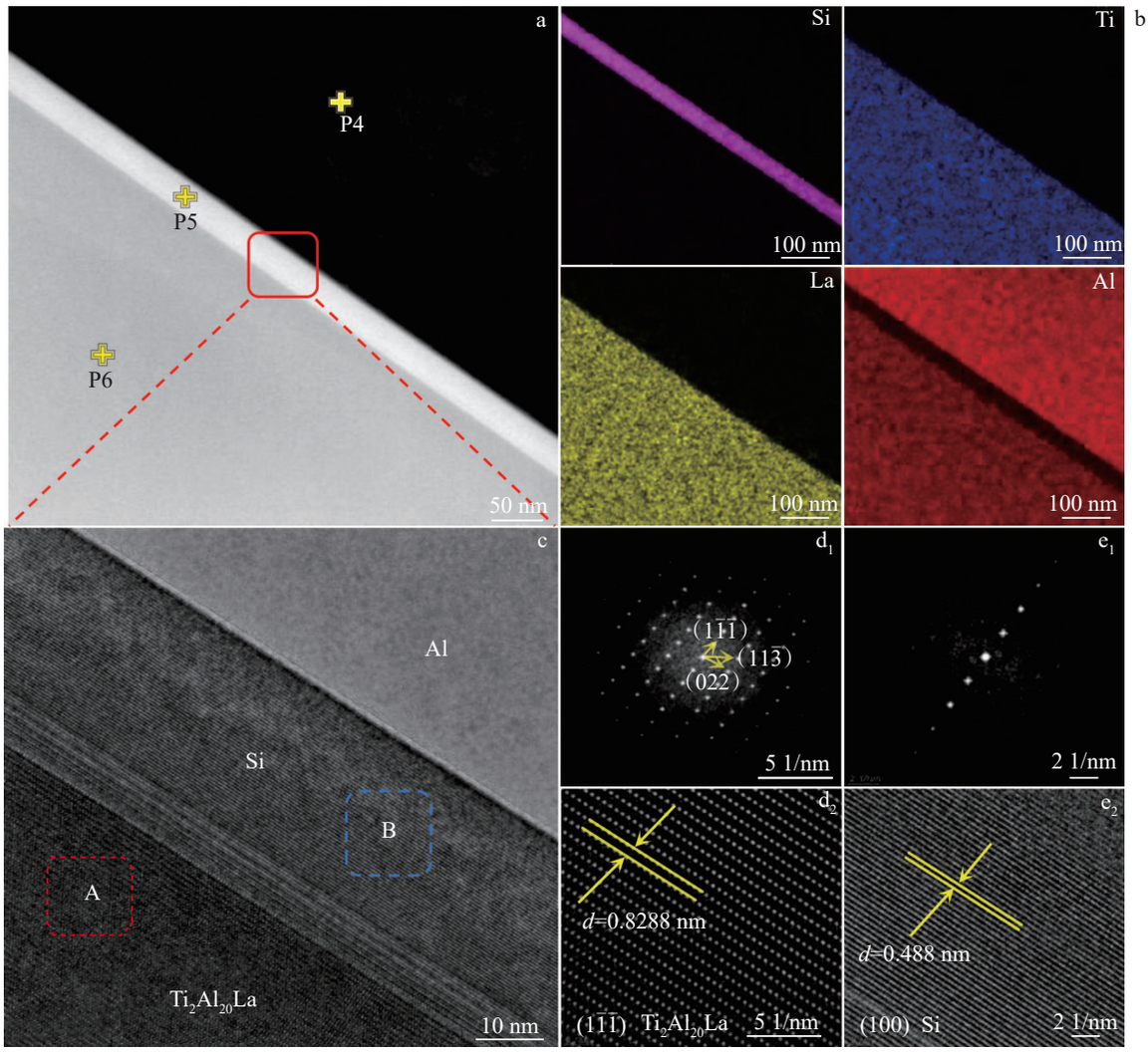

Fig.12 TEM image of interface between $Ti_2Al_{20}La$ phase and Al matrix (a) and corresponding EDS element mapping results (b); high-resolution TEM image of Si transition layer (c); SAED pattern (d_1) and lattice fringe (d_2) of $Ti_2Al_{20}La$ phase corresponding to area A in Fig.12c; SAED pattern (e_1) and lattice fringe (e_2) of Si phase corresponding to area B in Fig.12c

the primary reason for the effective contact between the rare-earth strengthened phase and the matrix interface. The enhanced interface contact facilitates the effective load transfer[31–33], mitigates stress concentration, and reduces the shedding of the strengthened phase during friction and wear[34]. Consequently, the enrichment of Si at the $Ti_2Al_{20}La$ phase interface enhances the toughness and wear resistance.

4 Conclusions

1) When 10wt% Al-Ti-La alloy is added to Al-7Si alloy, the eutectic Si in the prepared ($Ti_2Al_{20}La$+Al_3Ti)/Al-7Si composite is transformed from a needle-like structure of 17.00 μm in size to a rod-like structure of 8.78 μm in size. Furthermore, the α-Al is refined into equiaxed and columnar crystals of the smallest length of 31.6 μm, and the $Ti_2Al_{20}La$ and Al_3Ti strengthening phases are distributed in the matrix. However, when the Al-Ti-La content is excessively high, the large-scale $Ti_2Al_{20}La$ phase remaining in the alloy can lead to stress concentration and the formation of microcracks, which are detrimental to the material properties.

2) The grain refinement strengthening effect, secondary phase strengthening effect, and microstructure improvement effect of $Ti_2Al_{20}La$ and Al_3Ti phases greatly improve the mechanical properties of the composites. In comparison with those of the Al-7Si alloy, the tensile strength, elongation, and hardness of the ($Ti_2Al_{20}La$+Al_3Ti)/Al-7Si composite containing 10wt% Al-Ti-La alloy are enhanced by 13.4%, 57.0%, and 26.2%, respectively. The composite exhibits high strength and plasticity. In comparison with Al-7Si alloy, the composite demonstrates a 20% enhancement in wear resistance.

3) The high interfacial energy at the boundary between the reinforcement phase Al_3Ti and the aluminum matrix leads to the lattice distortion, forming a transition layer that is semi-coherent with the Al_3Ti phase. Furthermore, the element La enhances the adsorption of Si by the $Ti_2Al_{20}La$ reinforcement phase, leading to the accumulation of Si at the edge of the $Ti_2Al_{20}La$ phase and the formation of a semi-coherent Si layer.

The Al_3Ti transition layer and the Si-rich layer enhance the elongation and wear resistance of the composites.

References

1 Zhao L G, Li J H, Guo H J *et al*. *Rare Metal Mat Eng*[J], 2024, 53(3): 643
2 Kumar H G, Prashantha M, Xavior A *et al*. *Materials Letters*[J], 2021, 282: 128688
3 Anuar N F B W, Salleh M S, Omar M Z *et al*. *Mater Sci*[J], 2022, 9(5): 733
4 Li P X, Cai R, Yang G *et al*. *Mater Sci Eng A*[J], 2021, 823: 141749
5 Kar A, Sharma A, Kumar S. *Crystals*[J], 2024, 14(5): 412
6 Yang Qian, Zhang Jianxun, Sun Miao *et al*. *Rare Metal Mat Eng*[J], 2024, 53(8): 2343 (in Chinese)
7 Shah C, Raiyani D, Dave H *et al*. *Metallofiz Noveishie Tekhnol*[J], 2022, 44(5): 659
8 Chak V, Chattopadhyay H. *Mater Sci Technol*[J], 2021, 37(5): 467
9 Anuar N F B W, Omar M Z, Salleh M S *et al*. *J Mater Res Technol*[J], 2024, 30: 4813
10 Khobragade N, Roy D. *Int J Mater Res*[J], 2025, 116(2): 65
11 Sharma V K, Kumar V, Joshi R S. *J Mater Res Technol*[J], 2019, 8(4): 3504
12 Sharma V K, Kumar V, Joshi R S. *Mater Res Express*[J], 2019, 6(8): 865
13 Akbari M K, Baharvandi H R, Shirvanimoghaddam K *et al*. *Materials & Design*[J], 2015, 66: 150
14 Shivamurthy R C, Surappa M K. *Wear*[J], 2011, 271(9–10): 1946
15 Xiang Y L, Ma Y. *J Mater Eng Perform*[J], 2025, 49(1): 20
16 Xu Fusong, Geng Haorao, Wang Shouren. *Rare Met Mater Eng*[J], 2009, 38(2): 361 (in Chinese)
17 Peng J H, Deng Y F, He J T. *Adv Mater Res*[J], 2011, 311: 1017
18 Ding W W, Gou L M, Hu L W *et al*. *J Alloys Compd*[J], 2022, 929: 167350
19 Fang X G, Zhang T Y, Dong B K *et al*. *J Mater Res Technol*[J], 2024, 30: 1822
20 Xu C, Xiao W L, Zhao W T *et al*. *J Rare Earths*[J], 2015, 33(5): 553
21 Xia G Q, Zhao Q, Ping X C *et al*. *J Mater Res Technol*[J], 2024, 30: 1458
22 Ding W W, Xu M, Gou L M *et al*. *Metall Mater Trans A*[J], 2024, 55(9): 3617
23 Wang Y M, Du J L, Xiao H. *J Mater Res Technol*[J], 2023, 27: 4541
24 Qiu C R, Miao S N, Li X R *et al*. *Materials & Design*[J], 2017, 114: 563
25 Bhardwaj J, Vaidya A M, Meshram P D *et al*. *Int J Interact Des M*[J], 2024, 18(5): 2911
26 Pang J C, Fan G H, Cui X P *et al*. *Mater Sci Eng A*[J], 2013, 582: 294
27 Pu Z N, Zhang Y S, Kang X *et al*. *Ceram Int*[J], 2024, 50(9): 16000
28 Lu T, Pan Y, Wu J L *et al*. *Int J Min Met Mater*[J], 2015, 22: 405
29 Shibata N, Painter G S, Satet R L *et al*. *Phys Rev B: Condens Matter Mater Phys*[J], 2005, 72(14): 140101
30 Kuang Z Y, Xia Y X, Ju B Y *et al*. *Mater Sci Eng A*[J], 2024, 893: 146123
31 Mao F, Guo A Z, Zhang P *et al*. *Met Mater Int*[J], 2024, 30: 3458
32 Zhang T T, Feng K, Li Z G *et al*. *Appl Surf Sci*[J], 2020, 530: 147051
33 Yang S J, Yu J, Yao C L *et al*. *J Alloys Compd*[J], 2022, 903: 16387
34 Feng Y Q, Feng K, Yao C W *et al*. *Metall Mater Trans A*[J], 2019, 50: 3414

$(Ti_2Al_{20}La+Al_3Ti)$/Al-7Si复合材料的显微组织、力学性能和耐磨性能

安家志[1,2]，刘泉锋[1,2]，丁万武[1,2]，魏国立[3]，余海存[1,2]，杨成亮[3]

(1. 兰州理工大学 冶金与环境学院，甘肃 兰州 730050)

(2. 兰州理工大学 省部共建有色金属先进加工与再利用国家重点实验室，甘肃 兰州 730050)

(3. 酒泉钢铁(集团)有限责任公司，甘肃 嘉峪关 735100)

摘　要：采用熔配法制备了富含$Ti_2Al_{20}La$和Al_3Ti增强相的$(Ti_2Al_{20}La+Al_3Ti)$/Al-7Si复合材料，研究了不同Al-Ti-La合金添加量对复合材料的显微组织、力学性能及耐磨性能的影响。结果表明：向Al-7Si合金中加入10wt% Al-Ti-La合金得到的$(Ti_2Al_{20}La+Al_3Ti)$/Al-7Si复合材料由细小的α-Al晶粒、短棒状共晶Si、块状Al_3Ti及$Ti_2Al_{20}La$相所组成。复合材料的抗拉伸强度、延伸率、硬度分别为176.9 MPa、11.62%、73.2 HV，与Al-7Si合金相比，分别提高了13.4%、57.0%、26.2%，具有较高的强塑性，此外复合材料的耐磨性能也提高了20.1%。复合材料性能的提升有两方面影响因素。一方面是由于强化相Al_3Ti与铝基体交界处形成了Al_3Ti过渡层，且该过渡层与Al_3Ti呈半共格关系。另一方面，强化相$Ti_2Al_{20}La$中的La元素能够吸附Si元素，导致Si元素富集在$Ti_2Al_{20}La$相边缘，形成半共格的Si层。

关键词：铝基复合材料；Al-Ti-La合金；力学性能；耐磨性能

作者简介：安家志，男，1991年生，博士，兰州理工大学冶金与环境学院，甘肃 兰州 730050，E-mail：an_jzh@lut.edu.cn